An efficient Co-Ni hydrous oxide catalyst for elimination of NO pollutant in semi-enclosed spaces at ambient temperature

Bo Lin [a], Ziwei Bao [a], Aiyong Wang [a,*], Yuanqing Ding [a], Wangcheng Zhan [a], Li Wang [a,*], Yun Guo [a], Qiguang Dai [a], Yanglong Guo [a,*], Feng Gao [b,*]

[a] *State Key Laboratory of Green Chemical Engineering and Industrial Catalysis, Research Institute of Industrial Catalysis, School of Chemistry and Molecular Engineering, East China University of Science and Technology, Shanghai 200237, PR China*
[b] *Institute for Integrated Catalysis, Pacific Northwest National Laboratory, P.O. Box 999, Richland, WA 99352, United States*

ARTICLE INFO

ABSTRACT

Co-Ni bimetallic hydrous oxides are applied for the abatement of low-concentration nitric oxide (NO) pollution in semi-enclosed spaces. The textural properties of these materials are characterized by surface area/porosity analyzer, SEM/TEM imaging coupled with elemental mapping. In situ DRIFTS, XPS and temperature-programmed desorption are applied to elucidate the NO trapping mechanisms. The NO storage capacity is tested by flowing low-concentration NO in O_2/He through these materials at ambient temperature. The Co/Ni molar ratio is found to greatly influence the surface area, pore structure and morphology of the Co-Ni bimetallic hydrous oxides, thus affecting the elimination performance of low-concentration NO. During NO storage, nitrite formation is found to be associated with Co, and nitrate formation is found to be associated with Ni. In the Co-Ni bimetallic materials, a synergy exists where nitrite formed on Co is further oxidized to nitrate by lattice oxygen on Ni. Finally, these materials are readily regenerated by washing with $Na_2S_2O_8$ aqueous solution.

1. Introduction

Even though the transportation industry is rapidly evolving from traditional fuels to electrification, the majority of heavy duty on-road transportation at present still relies on fossil fuel powered internal combustion engines. As such, NO_x (nitrogen oxides, primarily NO) present in engine exhausts will continue to be a major source of air pollution in the near future even with the deployment of highly efficient NO_x abatement techniques, e.g., lean NO_x trap (LNT) and selective catalytic reduction (SCR). Particularly, such techniques are inefficient under the so-called "cold start" conditions [1–3]. With the world economy keeps booming, the demand for indoor parking and road tunnel, particularly in metropolitan areas, keeps increasing. In such semi-enclosed spaces, NO_x from engine exhausts can readily accumulate in air. If left untreated, NO_x concentration can reach tens of ppm, which is considered as a severe environment and human health hazard [4–8]. Because of the two major technical challenges, including (1) the large volumes of air to be treated, and (2) the low NO_x concentration that is inherent to this type of air pollution, highly efficient and economic techniques for eliminating low concentrations of NO_x in air have not

been materialized. Recent investigations suggest that this can be achieved by the two following mechanisms: First, NO_x-containing air passes through catalysts where NO is oxidized to gas phase NO_2, then NO_2 is absorbed by water or a basic solution [9–11]. Second, NO_x-containing air passes through solid materials where NO_x is activated and then adsorbed [12,13]. Since such materials provide both NO activation and trapping functionalities, they are called catalysts or adsorbers interchangeably in the present study. Note that the methods described above adopt the same principle as the LNT technique which utilizes trapping materials containing two phases: a noble metal phase for NO oxidation to NO_2, and an oxide phase (typically BaO) for NO_2 trapping [12,13]. However, NO_2 does not have to be an intermediate during ambient temperature NO trapping on the catalysts/adsorbers.

For economic reasons, the NO_x elimination methods described above must operate at ambient temperatures and at high space velocities. In recent years, researchers discovered a few transition metal oxides/hydroxides for this application, and best efficiencies have been realized on Mn-, Cr- and Co-based materials [14–22]. Table 1 summarizes the preparation methods of these materials and their NO trapping performance. Among them, Cr-X (X = Zr, Co, Fe, Ni) mixed oxides synthesized

---

Table 1
NO removal performance of selected catalysts/absorbers at ambient temperature.

Samples	Preparation method	WHSV[a] $(mL·g^{-1}·h^{-1})$ / GHSV[b] (h^{-1})	100% NO elimination time (h)	Reference
Mn-X composite oxides (X = Fe, Co, Ni, Zn)	Coprecipitation	120,000[a]	4	[14,15]
MnO_x	Redox precipitation	120,000[b]	20	[16]
Co_3O_4	Ammonia precipitation	120,000[a]	2	[17]
CrO_x	Ammonia precipitation	86,400[b]	8	[18]
Cr-X composite oxides (X = Zr, Co, Fe, Ni)	Sol-gel	45,000[a]	26	[19,20]
CoOOH	Redox precipitation	120,000[a]	6	[21]
Co/C	ZIF-67 carbonization	120,000[a]	15	[22]
$Co_xNi_yO_z·nH_2O$	Redox precipitation	120,000[a]	30	This work

by a sol-gel method, and poorly crystalline MnO_x oxides formed by redox precipitation display performance superior to others. Unfortunately, practical application for Cr-based catalysts is restricted owing to the high toxicity of chromium. MnO_x oxides, on the other hand, have not been demonstrated to be readily regenerated and reused at low costs.

In the past few years, our group focused on Co-based materials which are both non-toxic and readily regenerated after use. Our group first investigated NO removal on a Co/C material derived from pyrolysis of ZIF-67 in an inert atmosphere. This material shows remarkable efficiency for NO adsorption without formation of gas phase NO_2 for many hours [22]. Later, our group discovered that CoOOH formed using $Na_2S_2O_8$ as an oxidizing agent is also active for low-concentration NO removal at ambient temperature [21]. Unfortunately, the 100% NO removal efficiency for this material is much lower than our Co/C material tested under the same conditions. Herein, we report that by introducing Ni into CoOOH to form Co-Ni bimetallic hydrous oxides, NO trapping efficiency can be greatly improved. In addition to the high efficiency, the regeneration of the used Co-Ni bimetallic hydrous oxides is realizable via a simple approach. Particularly, high temperature calcination is never involved during the synthesis, use, and regeneration of these materials, avoiding secondary pollution. It is our understanding that the low cost, outstanding performance, ready preparation and regeneration make these Co-Ni bimetallic hydrated oxides the most compelling state-of-the-art candidates for low-concentration NO elimination from air at ambient temperatures.

2. Experimental

2.1. Material synthesis

The material preparation process contained two steps. The first step was co-precipitation. Designated amounts of $CoSO_4·7H_2O$ and $NiSO_4·7H_2O$ were dissolved in deionized water as the precursor solution, and Na_2CO_3 was dissolved in deionized water as the precipitation agent. Under stirring, the latter solution was dropwise added into the former at 30 °C. After continuous stirring for 1 h, the resultant precipitate was filtered, washed, and dried in a vacuum oven at 60 °C for 4 h. The second step was redox treatment/activation. The precipitate obtained in the first step was redispersed in deionized water under stirring for 30 min, during which the temperature was raised to 60 °C. $Na_2S_2O_8$ solution was dropwise added into the suspension under vigorous

stirring. The mixture was maintained at 60 °C under stirring for 48 h, before the black precipitate was filtered, washed, and dried at 80 °C for 4 h. Materials containing only Co or Ni were prepared following the same procedure. The final products were denoted Co-pure, Ni-pure and Co_xNi_y, where x and y represent the Co and Ni molar ratio of the corresponding precursor solution. A detailed example is provided as follows for the preparation of Co_1Ni_1. In the first step, 2.81 g (0.01 mol) $CoSO_4·7 H_2O$ and 2.81 g (0.01 mol) $NiSO_4·7 H_2O$ were dissolved in 20 mL of water, and 20 mL of 0.6 M Na_2CO_3 solution was used for precipitation. In the second step, 2.38 g of precipitate was redispersed in 20 mL of H_2O, then 20 mL of 0.75 M $Na_2S_2O_8$ was added. All samples were ground, pressed and sieved to 40–60 mesh size before NO storage measurements. The chemical reactions involved in these processes can be described as $2 M^{2+} + 4OH^- + S_2O_8^{2-} \rightarrow 2SO_4^{2-} + 2MOOH\downarrow + 2 H^+$, where M = Co or Ni.

2.2. Material characterization

Textural and morphological properties of the samples were examined with surface area/porosity analyzer, XRD and SEM/TEM imaging coupled with elemental mapping. N_2 adsorption/desorption isotherm at 77 K, carried out on a Micromeritics ASAP 2020 M, was used to obtain surface area and porosity. Before the measurements, all samples were pretreated in high vacuum at 80 °C overnight. The Brunauer-Emmett-Teller (BET) method was used to calculate the specific surface area. XRD measurements were conducted on a Rigaku D/max2550VB/PC with Cu Kα radiation (40 kV, 100 mA, λ = 1.5406 Å). The diffraction patterns were collected with a scanning speed of 0.1°/s from 10° to 80°. Field emission scanning electron microscopy (SEM) images were acquired with a scanning electron microscope (Nova Nano SEM 450) after the samples were coated with a thin layer of evaporated gold. Transmission electron microscopy (TEM) analysis was conducted on a JEOL JEM-2100 electron microscope operated at 200 kV. The samples were first dispersed in ethanol and then deposited on copper grids covered with a carbon film.

The nature of the active phases in these samples was probed with TG-DTA, TPD, and Raman, in situ DRIFTS and XPS spectroscopies. TG-DTA was carried out on a PerkinElmer Diamond TG/DTA system in a flowing air with a flow rate of 50 mL/min and a heating rate of 10 °C/min from 30 °C to 600 °C. Raman spectra were collected using a Renishaw Invia Reflex laser micro-Raman spectrometer equipped with a CCD detector. The excitation wavelength of laser beam was 514 nm with a power of 1 mW at a resolution of 4 cm^{-1}. Each spectrum was a sum of two scans recorded from 300 to 3000 cm^{-1}. XPS measurements were performed on a Thermo ESCALAB 250Xi spectrometer with Al Kα (1486.6 eV) radiation as the excitation source in ultrahigh vacuum (6.7 × 10^{-8} Pa). Binding energies (BE) were corrected with respect to a C1s BE of 284.4 eV from adventitious carbon. The powder samples were pressed into self-supported disks loaded in the sub-chamber and evacuated for 4 h. The XPS spectra were deconvoluted and fitted by a Gaussian function with the XPSPEAK 4.1 software.

In situ DRIFTS and temperature-programmed desorption (TPD) were used to probe the nature of the stored N-containing species. In situ DRIFTS measurements were performed on a Nicolet Nexus 6700 FT-IR spectrometer with an MCT detector. Prior to each test, the samples were pretreated at 60 °C for 1 h (50 mL·min^{-1} of Ar as the balanced gas). Next, the samples were cooled to 25 °C and then reacted with the feed gas (500 ppm NO, 21 vol% O_2, Ar as the balance gas) with a total flow of 50 mL·min^{-1}. The spectra were collected with a sum of 60 scans at a spectral resolution of 4 cm^{-1}, and all spectra were obtained by subtracting background spectra collected prior to NO flow. TPD measurements were carried out on used samples after NO trapping tests for 50 h. Before temperature ramping, the samples were purged with flowing Ar (300 mL·min^{-1}) for 1 h at 25 °C. Following which, the samples were heated from 30 to 600 °C in the same Ar flow at a ramping rate of 5 °C/min, and maintained at 600 °C for 10 min for complete NO_x removal.

The concentrations of outlet NO and NO_2 were recorded in real time by a NO_x analyzer (Thermo Fisher 42i-LS).

2.3. NO removal evaluation

The NO removal performance tests of the samples were conducted in a continuous-flow fixed-bed quart reactor (i.d.=8 mm). 0.15 g catalyst (40–60 mesh) was used for each test and the reactant gas was composed by 10 ppm NO, 21% O_2 and the balanced argon. Total gas flow and gas hourly space velocity were 300 mL·min^{-1} and 120,000 mL·g^{-1}·h^{-1}, respectively. Before each test, the sample was pretreated at ambient temperature in a following argon (200 mL·min^{-1}) for 1 h. The inlet and outlet concentrations of NO and NO_2 were detected by the NO_x analyzer described above. NO removal ratio is calculated by the following equation:

$$NO \text{ } removal \text{ } ratio(\%) = \frac{NO_{inlet} - NO_{outlet}}{NO_{inlet}} \times 100\%$$

where the subscripts 'inlet' and 'outlet' represent the inlet and outlet NO concentrations, respectively.

2.4. Material regeneration

0.3 g used material (NO removal test for 50 h) was dispersed into 10 mL deionized water in a 25 mL round-bottom flask, forming a suspension. 10 mL (1 M) $Na_2S_2O_8$ was dropwise added into the suspension. The reaction temperature was held at 60 ℃ for 24 h with continuous magnetic stirring. After filtered, washed and dried at 80 ℃ for 4 h, the regenerated material was obtained.

3. Results and discussion

3.1. Effect of Co/Ni molar ratio on NO removal ratio

Fig. 1a shows low-concentration NO removal ratio as a function of time on-stream over Co-pure, Ni-pure, and Co-Ni hydrous oxides with different Co/Ni molar ratios (denoted as $Co_xNi_yO_z \cdot nH_2O$) at ambient temperature (Inlet NO and NO_2 concentrations are presented in Fig. S1). Real-time NO and NO_2 outlet concentrations are also included in Fig. S2 and Fig. 1b. Co-pure shows remarkable NO trapping efficiency, where 100 % NO elimination lasts for about 18 h. Note that when NO removal ratio drops below 100 % (i.e., when NO appears in the outlet), no NO_2 is detected in the outlet. In drastic contrast, Ni-pure displays poor NO trapping, where 100 % NO elimination only lasts for minutes. Moreover, as NO trapping efficiency declines, ~2 ppm NO_2 is detected in the outlet, corresponding to a NO_2 formation rate of 8.9◊10^{-7} mol·g^{-1}·min^{-1}. This demonstrates that, in contrast to Co-pure, Ni-pure is active in catalyzing NO oxidation to NO_2. For the $Co_xNi_yO_z \cdot nH_2O$ materials, dramatic effects of Co/Ni ratio are observed. Co_4Ni_1 displays 100 % NO elimination for ~28 h. As outlet NO starts to appear, NO_2 formation is also detected. It reaches a maximum of ~0.5 ppm at ~40 h, and then stabilizes at 0.2 ppm as the test continues. Co_1Ni_1 displays slightly improved efficiency where complete NO_x removal lasts for ~30 h. This catalyst generates higher concentrations of NO_2 which maximizes at ~50 h. Rather unexpectedly, the NO elimination performance for Co_1Ni_4 is even lower than Ni-pure, showing rapid decline of trapping efficiency and almost instantaneous NO_2 release during time on-stream.

The results shown in Fig. 1 demonstrate the following important points: (1) there exists clear synergy between CoOOH and NiOOH in the Co_xNi_y materials since the NO_x trapping efficiency for these materials is different from that expected from physical mixtures of Co-pure and Ni-pure. (2) NO_2 formation in the gas phase is clearly associated with the presence of Ni. To gain a better understanding about possible synergies between CoOOH and NiOOH, a number of characterization techniques
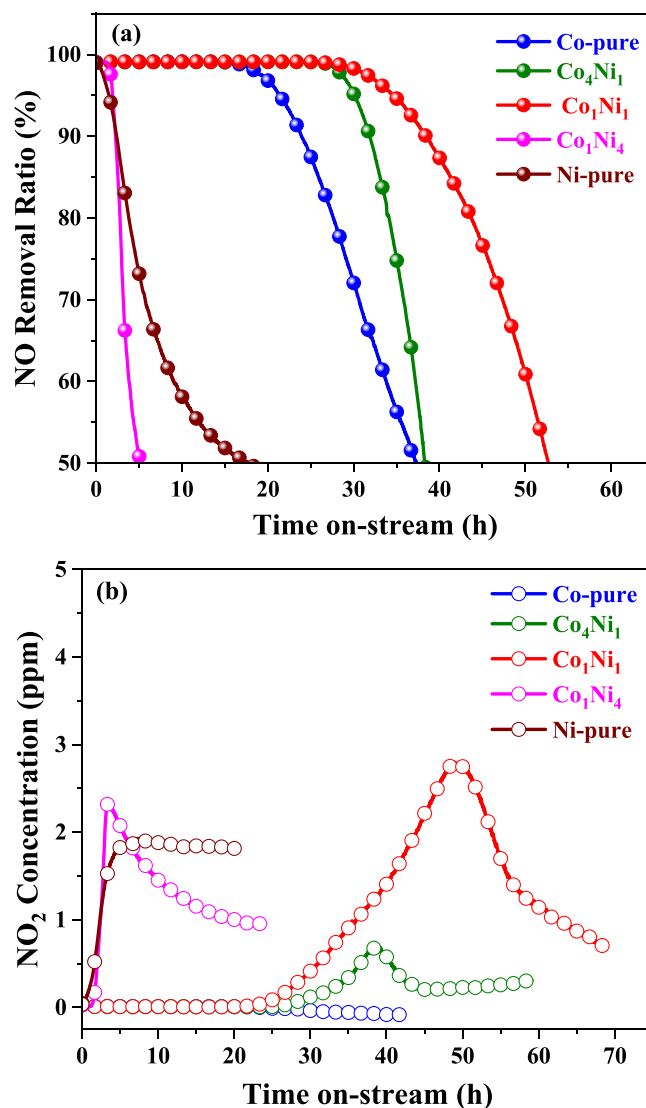

Fig. 1. NO removal ratio (a) and outlet NO_2 concentration (b) for $Co_xNi_yO_z \cdot nH_2O$ materials. The reactant feed gas contains 10 ppm of NO, 21 % of O_2 balanced with Ar at a WHSV of 120,000 mL·g^{-1}·h^{-1} and a reaction temperature of 25 ℃.

were applied, and the results are shown as follows.

3.2. Physicochemical properties of the materials

Based on the N_2 adsorption-desorption isotherms of the $Co_xNi_yO_z \cdot nH_2O$ materials, as illustrated in Fig. 2, Co-pure displays a microporous (type I) isotherm, Co_1Ni_4 displays a non-porous (type II) isotherm, and all three other materials (Co_4Ni_1, Co_1Ni_1 and Ni-pure) present type IV isotherms. The isotherms for Co-pure, Co_4Ni_1 and Co_1Ni_1 all display marked N_2 adsorption/desorption in the low-pressure regime ($P/P_0 < 0.1$), demonstrating their richness in microporous structures. Additionally, the isotherms for Co_4Ni_1, Co_1Ni_1 and Ni-pure display hysteresis loops of the H4 type, suggesting the accumulation of mesopores due to loosen stacking of layered structures. Table 2 presents specific surface areas, pore volumes and average pore sizes of the $Co_xNi_yO_z \cdot nH_2O$ materials. Co-pure possesses a relatively large surface area of 259 m^2/g and a small average pore size of 3.8 nm, slightly larger than the maximum pore size limit of 2 nm for microporous materials by definition. In contrast, Ni-pure has a smaller surface area of 93 m^2/g, and a much larger average pore size of 11.8 nm. These results are highly
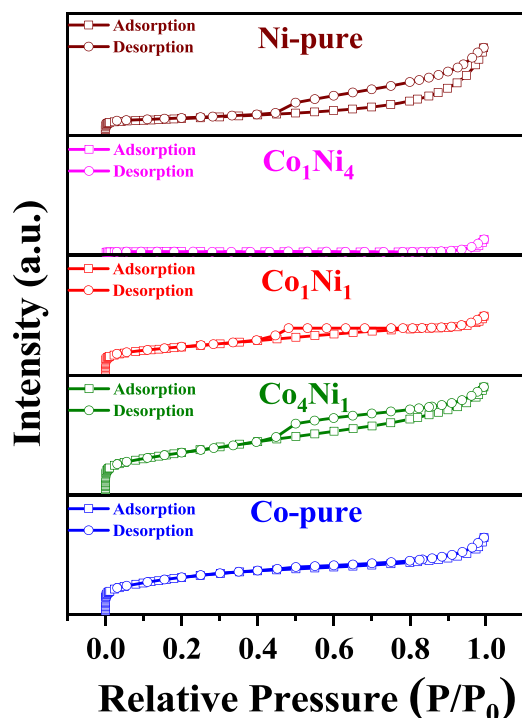
Fig. 2. Nitrogen adsorption-desorption isotherms for $Co_xNi_yO_z \cdot nH_2O$ materials.

Table 2
Specific surface area, pore volume and average pore size for $Co_xNi_yO_z \cdot nH_2O$ materials.

Samples	BET Surface area (m^2/g)	Pore volume (cm^3/g)	Average pore size (nm)
Co-pure	259	0.25	3.8
Co_4Ni_1	303	0.35	4.0
Co_1Ni_1	186	0.18	4.6
Co_1Ni_4	8	0.04	21.3
Ni-pure	93	0.28	11.8

Fig. 3. XRD patterns (a) and Raman spectra (b) for $Co_xNi_yO_z \cdot nH_2O$ materials.

consistent with the isotherms of the two materials shown in Fig. 2. Compared to Co-pure, the specific surface area of Co_4Ni_1 increases to 303 m^2/g and average pore size increases to 4.0 nm, suggesting the incorporation of Ni facilitates the formation of pore structure. With further incorporation of Ni into Co_1Ni_1, pore size further increases to 4.6 nm as expected; however, surface area decreases to 186 m^2/g somewhat unexpectedly. More surprisingly, the surface area of Co_1Ni_4 is only 8 m^2/g, much lower than the surface area of a physical mixture of Co-pure and Ni-pure at the same Co/Ni ratio. The poor NO_x storage efficiency for Co_1Ni_4 (Fig. 1), therefore, is due at least partly to its low surface area. It is important to note, however, that surface area is not the only physiochemical property that controls NO_x storage capacity. For example, Co_1Ni_1 displays improved NO removal performance than Co_4Ni_1, yet Co_1Ni_1 only has a surface area ~60 % that of Co_4Ni_1. Furthermore, Ni-pure has a surface area ~50 % that of Co_1Ni_1, yet its NO_x removal performance much worse than Co_1Ni_1. The presence of Co is obviously critical for high NO_x storage. To gain more knowledge on the chemical nature and local environment of the Co species in these materials, additional characterizations were conducted, and the results are presented below.

Fig. 3a and Fig. 3b display the XRD patterns and Raman spectra for the $Co_xNi_yO_z \cdot nH_2O$ materials, respectively. The diffractogram for Co-pure can be indexed to CoOOH ($2\theta = 20.24°$, $38.89°$, $65.34°$ and $68.37°$). However, the low peak intensity and broad peak width indicate that this material is poorly crystalline. The Raman spectra for this
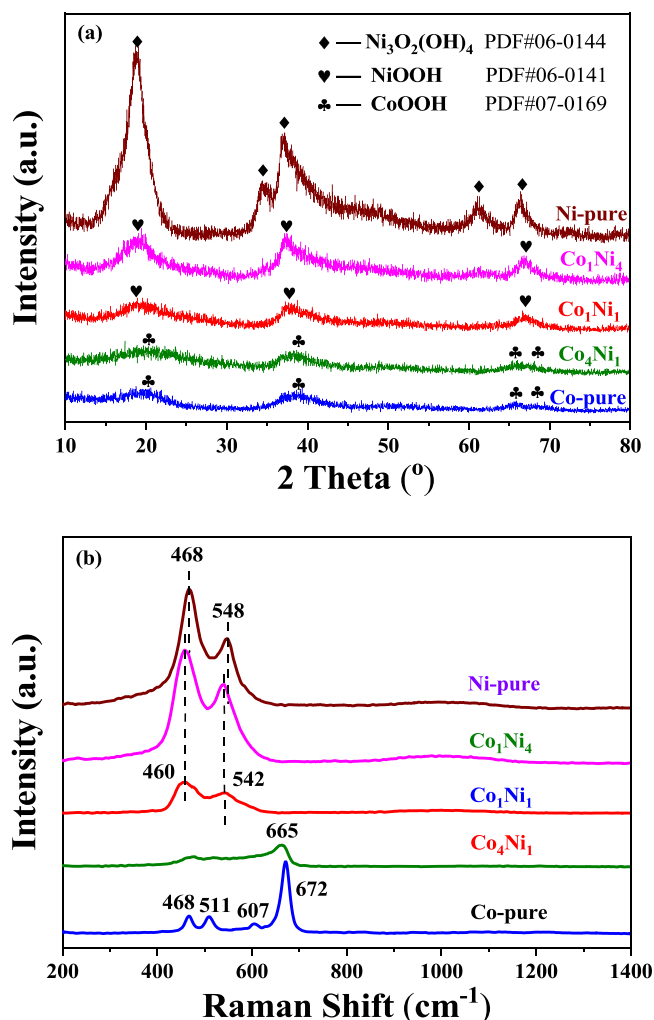
material, however, displays shifts that are readily assigned to Co_3O_4. This discrepancy is ascribed to laser induced dehydration of unstable CoOOH during Raman measurement [23]. The XRD patterns for Ni-pure display stronger intensities than Co-pure, suggesting that this material has higher crystallinity than the latter. The XRD patterns are readily indexed to $Ni_3O_2(OH)_4$; based on this stoichiometry, the average valence for nickel is + 8/3. Therefore, Ni adopts both + 2 and + 3 oxidation states. The Raman spectrum for Ni-pure displays two strong shifts: a Ni^{3+}-O bending vibrational peak at 468 cm^{-1} and a Ni^{3+}-O stretching vibrational peak at 548 cm^{-1} [24,25]. The XRD patterns and Raman spectra for the Co_xNi_y materials display unique features which are dissimilar to physical mixtures of Co-pure and Ni-pure. Particularly, while Co_4Ni_1 displays XRD patterns which are similar to Co-pure, Co_1Ni_1 and Co_1Ni_4 display patterns which are readily indexed to NiOOH. Likewise, Co_4Ni_1 displays Raman shifts which are similar to Co-pure but with much weaker signals suggesting less significant laser induced Co_3O_4 formation. In contrast, both Co_1Ni_1 and Co_1Ni_4 display Raman shifts at 460 and 542 cm^{-1}, consistent with the presence of NiOOH in these materials. Notably, these vibrations are similar to those of Ni-pure but red-shifted about 8 cm^{-1}. Such a difference can be attributed to the additional Ni^{2+}-O vibrations in the $Ni_3O_2(OH)_4$. The XRD and Raman results shown here strongly suggest that during co-precipitation, CoOOH and NiOOH mix intimately forming uniform and poorly crystalline mixtures. In the next, SEM and TEM were applied to better understand the textures of these materials.

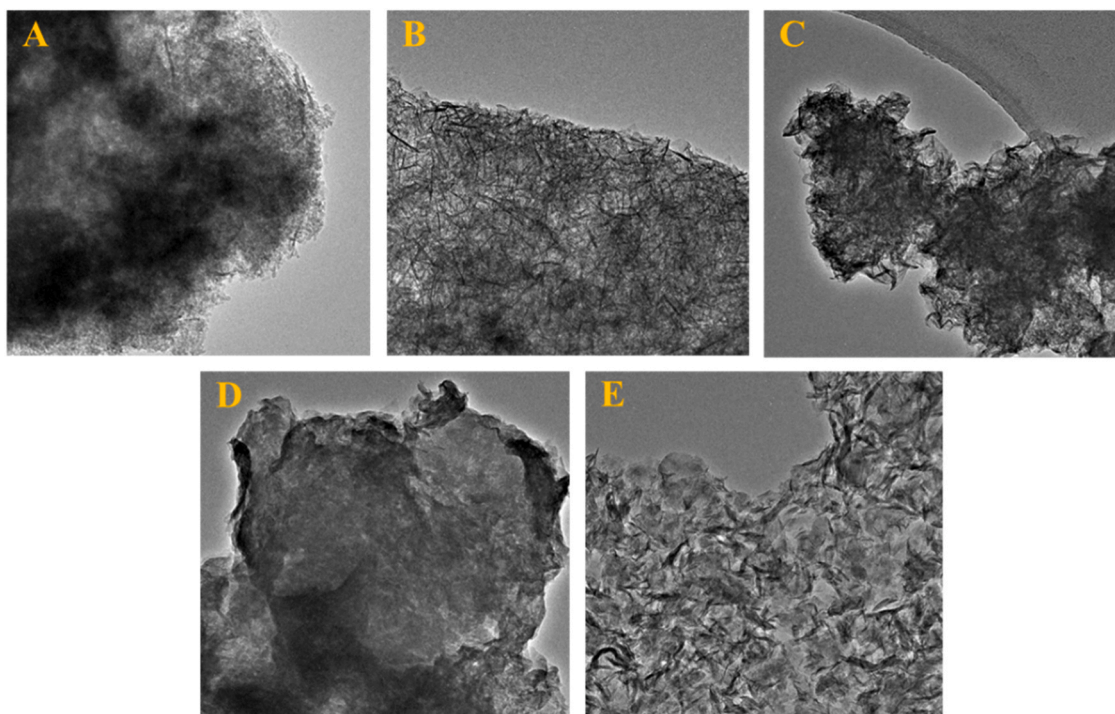Fig. 4(a-e) present TEM images of the $Co_xNi_yO_z \cdot nH_2O$ materials. As

**Fig. 4.** TEM (A-E) images for $Co_xNi_yO_z \cdot nH_2O$ materials.

shown in Fig. 4a, Co-pure mainly contains aggregation of near-spherical particles, and some sheet-like structures are also observed. It is likely that the aggregation of the fine grains forms the near-microporous structure. Unlike Co-pure, Fig. 4e shows that Ni-pure primarily adopts a crumpled sheet structure. The sheets do not appear to have an orientation. The porosity data shown in Table 2 suggests that the voids between sheets are mesoporous in nature. Interestingly, as show in Fig. 4b, Co_4Ni_1 primarily contains curly sheets, but with thicknesses much thinner than those shown in Fig. 4e for Ni-pure. This result demonstrates that the growth pattern of CoOOH becomes, at least partially, governed by the growth pattern of NiOOH during co-precipitation. Some CoOOH in this material may still adopt spherical grain structures, however, this cannot be resolved from the image. With increasing Ni content, Co_1Ni_1 develops curly sheets (Fig. 4c) which are thicker than those in Co_4Ni_1, but thinner than those in Ni-pure. Such a tread is well reflected from the surface area/porosity data shown in Table 2. Again, it is difficult to determine whether spherical CoOOH particles are still present in this material. For Co_1Ni_4, individual sheets are no longer crumpled, but are instead stacked layer by layer forming large, non-porous particles (Fig. 4d). The TEM images shown in Fig. 4 suggest again that CoOOH and NiOOH are intimately mixed in the Co_xNi_y samples. Otherwise, (1) the growth pattern of CoOOH should not have been so greatly influenced by the growth of NiOOH, and (2) the stacking of layers in Co_1Ni_4 should not have been so much denser than Ni-pure. This notion is further proven by STEM-mapping data for Co_4Ni_1 shown in Fig. 5, where both Co and Ni are uniformly dispersed. For Co_1Ni_1 and Co_1Ni_4, uniform Co and Ni dispersion is also found, and the data are presented in the Supplementary information (Fig. S3). SEM images of the $Co_xNi_yO_z \cdot nH_2O$ materials are also shown in Fig. S4. Due to their limited resolution, these images are less revealing than the TEM images.

To achieve a molecular level understanding how these $Co_xNi_yO_z \cdot nH_2O$ materials eliminate NO in the gas phase, their chemical nature should be well understood. Even though XRD and Raman characterizations (Fig. 3) provide important information in this regard, the poorly crystalline nature of these materials (except Ni-pure) precludes a simple conclusion that CoOOH and NiOOH are the only chemicals which are present. In the following, these materials were further analyzed with

TGA and XPS.

Fig. 6 displays TGA profiles of these materials. Co-pure and Co_4Ni_1 display nearly liner weight losses from 30 to ~250 °C. Above this temperature, weight losses become much slower. From 30 to ~200 °C, Ni-pure and Co_1Ni_4 show slower weight losses than Co-pure and Co_4Ni_1, but become comparable to them in the ~200–300 °C range. Again, weight losses for Ni-pure and Co_1Ni_4 become much slower at higher temperatures. The weight loss behavior for Co_1Ni_1 lies in between of these two cases. In principle, pure CoOOH (or NiOOH) conversion to CoO (or NiO) should result in a weight loss of ~19 %. Obviously, all materials have weight losses substantially higher than that, suggesting the presence of structural water and/or OH^-/M (M = Co, Ni) molar ratios higher than unity in these materials.

Fig. 7(a-c) display Co 2p, Ni 2p and O 1s XPS spectra for the $Co_xNi_yO_z \cdot nH_2O$ materials, respectively. As the cobalt content declines, the peak area of Co 2p 3/2 and Co 2p 1/2 gradually decreases. However, the binding energies for Co 2p 3/2 and Co 2p 1/2 do not shift with Co/Ni ratio. Concurrently, the peak areas for Ni 2p 3/2 and Ni 2p 1/2 gradually increase but again, the binding energies do not shift. The Co 2p 3/2 binding energy of 780.2 eV and the Ni 2p 3/2 binding energy of 855.8 eV fully reproduce previously measured data on CoOOH [26,27], and NiOOH or $Ni_3O_2(OH)_4$ [28,29], respectively. The results demonstrate that CoOOH and NiOOH in the Co_xNi_y samples do not electronically perturb each other, even though their proximity obviously influences the growth pattern during co-precipitation synthesis (Fig. 4). The O 1s region spectra are readily deconvoluted into three components, corresponding to different oxygen species. O_α at the binding energy of 529.4–529.7 eV is ascribed to lattice oxygen (e.g., Co-O-Co or Ni-O-Ni). O_β at the binding energy of 530.9–531.1 eV belongs to hydroxyl oxygen (e.g., Co-O-H or Ni-O-H). O_γ at the binding energy of 532.3 eV is attributed to surface absorbed oxygen species [30–32]. With increasing Ni content in these materials, the binding energies for O_α and O_β shift to lower values, indicating that Co cations have stronger bindings of these oxygen atoms than Ni cations. This is likely the reason why NO_2 in the gas phase only forms on the materials containing Ni (Fig. 1).
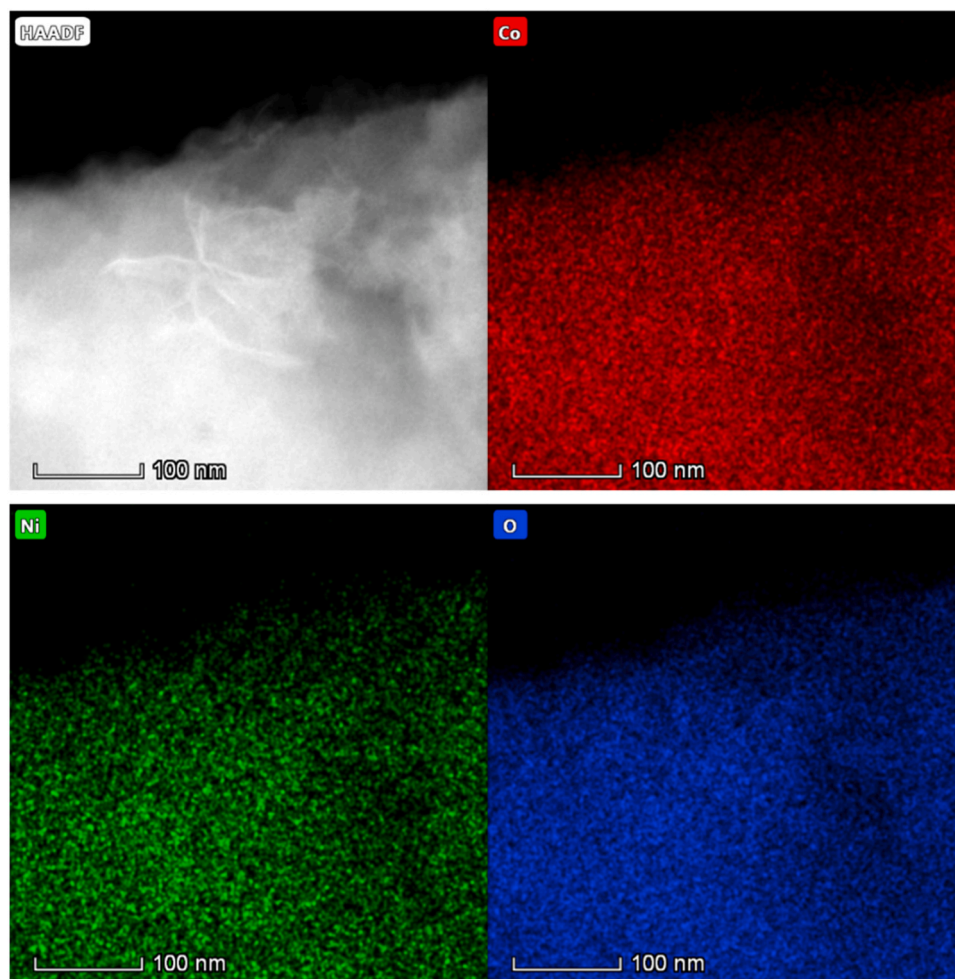
Fig. 5. STEM-mapping on Co_4Ni_1 material.
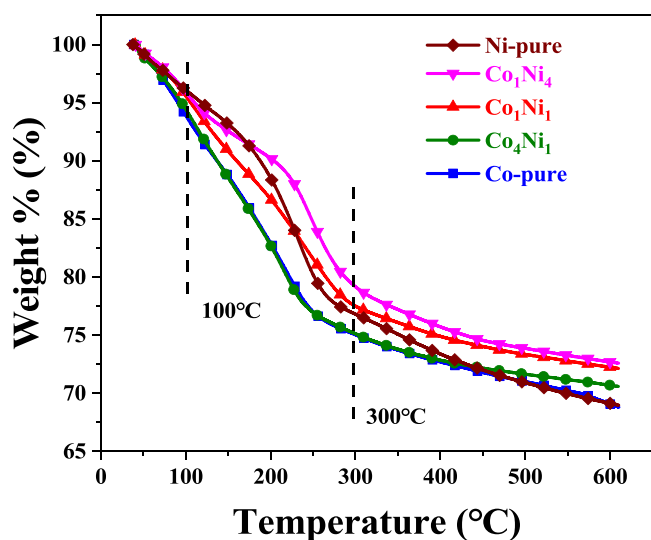
Fig. 6. TG profiles for $Co_xNi_yO_z \cdot nH_2O$ materials.

3.3. Mechanisms for NO elimination

A combination of XPS, DRIFTS and TPD were utilized to study the NO storage mechanism over the $Co_xNi_yO_z \cdot nH_2O$ materials. XPS was first used to compare samples before and after NO adsorption for 50 h in the Co 2p 3/2, Ni 2p 3/2, O 1s and N 1s regions. As shown in Fig. 8a, the Co 2p 3/2 features for all materials shift to higher binding energies after NO adsorption. Since Co^{3+} displays a rather unique binding energy decrease as compared to Co^{2+} [33,34], such changes confirm that Co^{3+} in the material becomes reduced to Co^{2+} via the NO elimination reactions. The extents of the chemical shifts follow the order $Co_1Ni_1 > Co_4Ni_1 > Co$-pure $> Co_1Ni_4$, correlating positively with NO removal efficiency of these materials (Fig. 1). Fig. 8b shows the Ni 2p 3/2 region spectra. For Ni-pure, the binding energy shifts slightly to lower value after NO adsorption indicating reduction of Ni^{3+} to Ni^{2+}. For the other three Co_xNi_y materials, no obvious changes are observed before and after the NO elimination reaction. As shown in Fig. 8c, both nitrate and nitrite species are detected, located at N 1s binding energies of 406.8 eV and 403.6 eV, respectively, over the Co-pure, Co_4Ni_1 and Co_1Ni_1 materials [35,36]. By comparing the signal peak areas, nitrate storage follows the order $Co_1Ni_1 > Co_4Ni_1 > Co$-pure, and nitrite storage follows the order Co-pure $> Co_4Ni_1 > Co_1Ni_1$. It is important to note that NO oxidation to nitrite and nitrate requires the participation of active oxygen species which bind to the metal cation sites. The lack of Ni 2p chemical shift in the Co_xNi_y materials before and after NO adsorption suggests that only oxygen bound to Co participates in NO activation. However, Ni also appears to play certain roles since the nitrate/nitrite selectivity obviously is influenced by Co/Ni ratios.

To gain further details on NO trapping, Fig. 9(a-e) presents the deconvoluted O 1s XPS spectra for Co-pure, Co_4Ni_1, Co_1Ni_1, Co_1Ni_4 and Ni-pure, respectively, before and after NO adsorption. In this case, the O 1s spectra were deconvoluted into three characteristic peaks for lattice
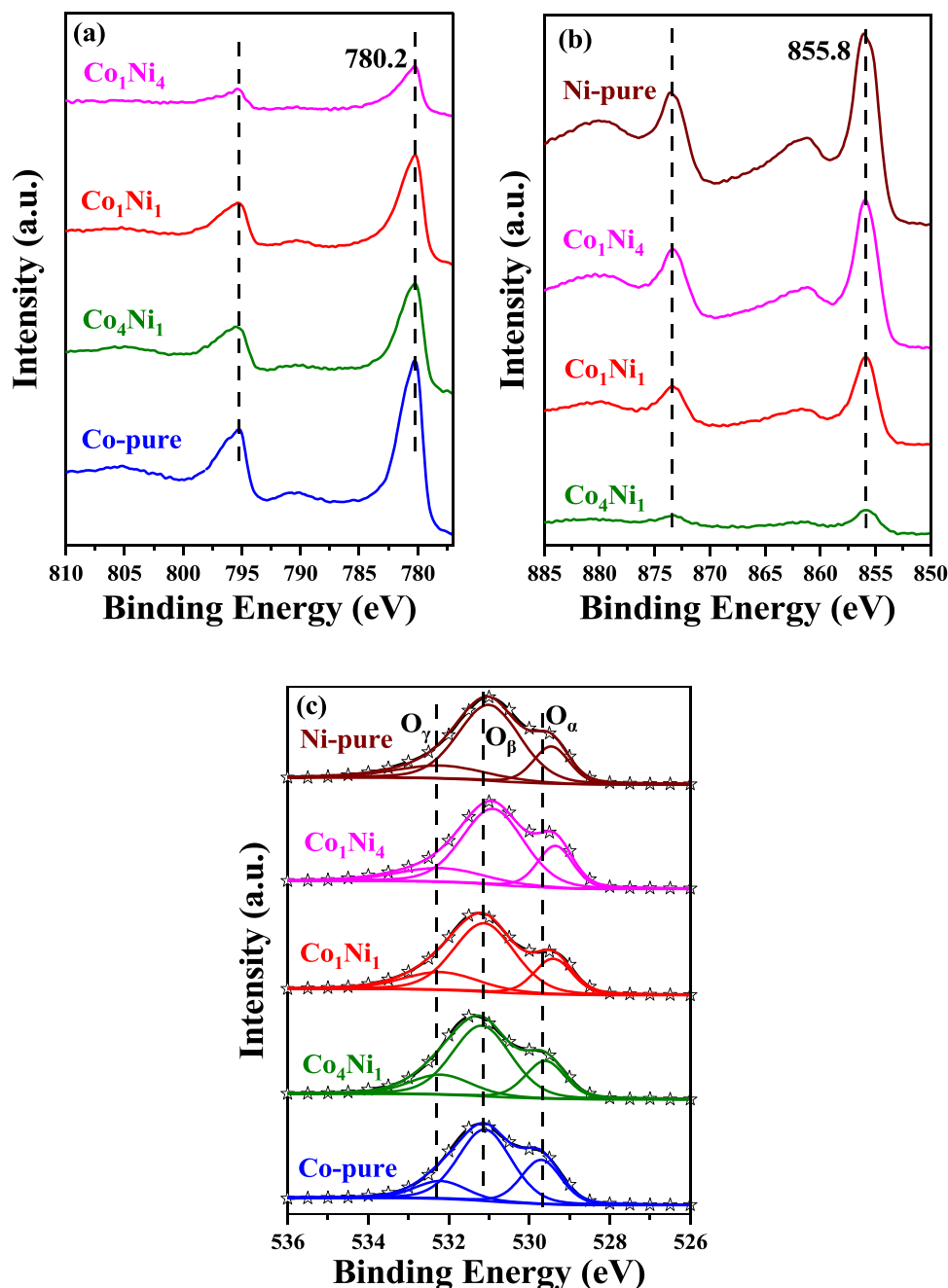
Fig. 7. Co 2p (a), Ni 2p (b) and O 1 s (c) region of XPS spectra for $Co_xNi_yO_z \cdot nH_2O$ materials.

oxygen (O_α), hydroxyl oxygen (O_β) and surface adsorption oxygen species (O_γ), and their peak areas are tabulated in Table 3. After the NO trapping test, O_α contents in Co-pure, Co_4Ni_1, Co_1Ni_1 all decrease ($\Delta O_\alpha = -3.7$ %, -6.7 %, and -13.9 %, respectively). Clearly, lattice oxygen consumption increases when the Ni content increases in these materials. Notably, Ni-pure also consumes large amount of O_α ($\Delta O_\alpha = -11.7$ %) during NO trapping. On the other hand, substantial amounts of O_β in Co-pure, Co_4Ni_1, Co_1Ni_1 is consumed ($\Delta O_\beta = -12.9$ %, -12.6 %, and -11.1 %, respectively) during NO trapping, whereas that in Ni-pure is nearly unchanged ($\Delta O_\beta = -0.5$ %). These data demonstrate the much higher activity of hydroxyls bound to cobalt. For Co_1Ni_4, both O_α and O_β contents ($\Delta O_\alpha = -4.0$ %, $\Delta O_\beta = -3.5$ %) decline slightly after NO adsorption. The low efficiency is attributed to the exceedingly low surface area of this material, rendering low accessibility of O_α and O_β. Finally, the O_γ contents in Co-pure, Co_4Ni_1, Co_1Ni_1, Co_1Ni_4 and Ni-pure

increase 16.6 %, 19.3 %, 25 %, 7.5 % and 12.2 % after NO adsorption, corresponding to the following order from large to the small: $Co_1Ni_1 > Co_4Ni_1 >$ Co-pure $>$ Ni-pure $> Co_1Ni_4$. This order is in line with the NO elimination efficiency order shown in Fig. 1, suggesting that the O_γ increase is due to nitrate/nitrite formation, where the O 1s binding energies for these species are indistinguishable from that of the surface O_γ species prior to NO trapping.

In situ DRIFTS was performed to investigate the evolution of NO adsorption products. Fig. 10 (a-e) presents evolution of the characteristic IR bands recorded on Co-pure, Co_4Ni_1, Co_1Ni_1, Co_1Ni_4 and Ni-pure, respectively, during the first 30 min of NO adsorption (spectra recorded at 5-min intervals). For all samples, it is readily observed that new IR bands develop upon NO introduction, and intensify with increasing exposure time. For Co-pure, the strong bands observed at the 1337 cm^{-1} and 1415 cm^{-1} correspond to symmetrical and asymmetrical stretching
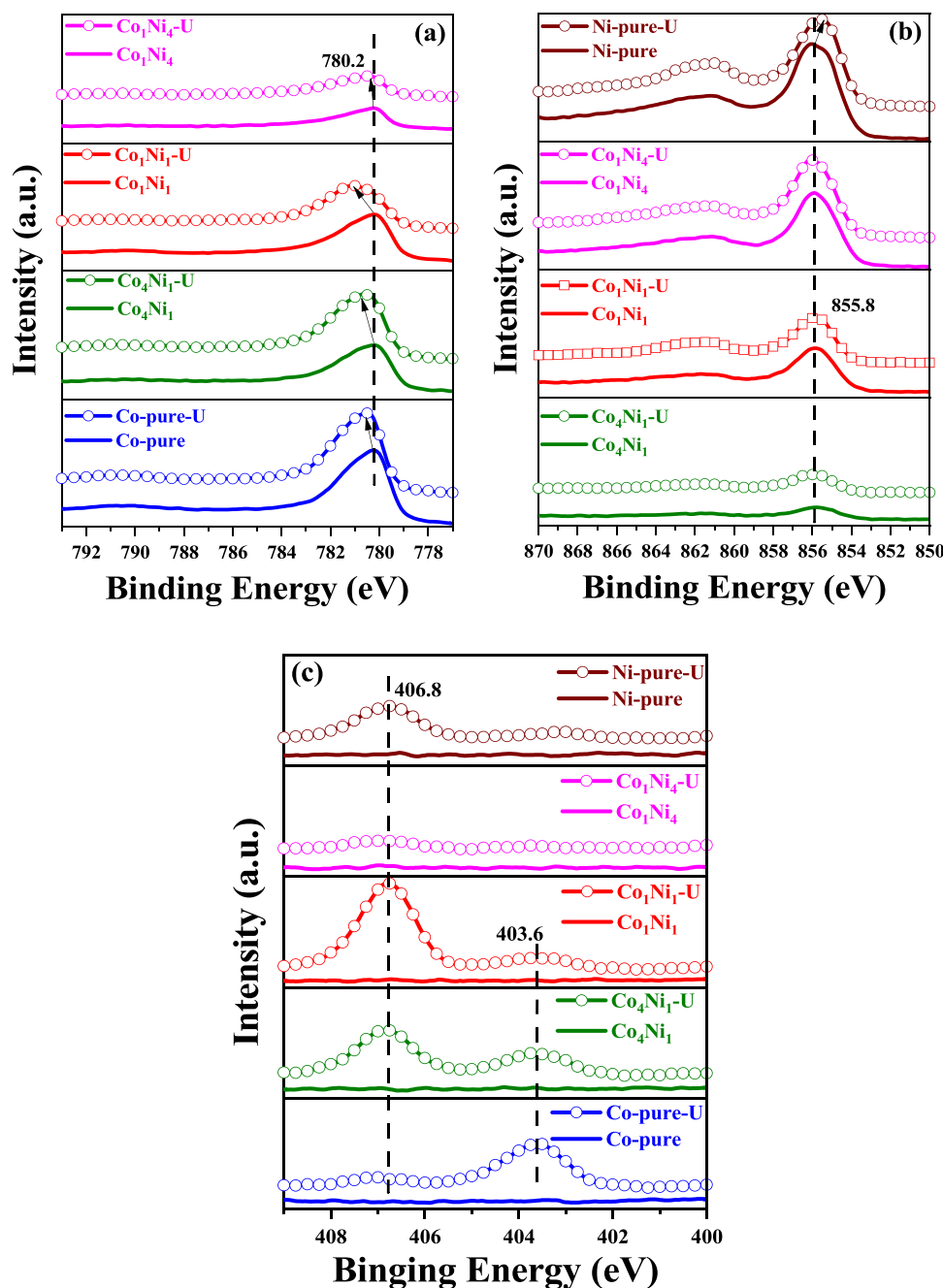
Fig. 8. Co 2p 3/2 region of XPS (a), Ni Co 2p 3/2 region of XPS (b), N 1 s XPS (c) spectra for fresh and used $Co_xNi_yO_z \cdot nH_2O$ materials.

of nitro complex (-NO_2) [37,38]. The weaker bands at 1190 and 1630 cm^{-1} can be assigned to chelating nitro compound [39] and bending vibration of H_2O [40], respectively. The detection of the nitro complexes is in line with the dominance of nitrite deposition on this sample as evidenced by XPS (Fig. 8c). For Co_4Ni_1, the most pronounced peaks are located at 1329 and 1420 cm^{-1}, similar to those on Co-pure. However, XPS spectra shown in Fig. 8c suggests that strong nitrate formation also occurs on this sample. Since ionic nitrates typically display split vibrational bands around 1420 and 1320 cm^{-1} and symmetric bending mode around 1030 cm^{-1} [41], the IR bands for nitro complexes are not readily distinguished from those of ionic nitrates. Hence, the bands at 1420, 1329 and 1030 cm^{-1} for Co_4Ni_1 are suggested to be contributed by both nitro compounds and ionic nitrates. Chelating nitro compound (ν = 1190 cm^{-1}) and water (ν = 1630 cm^{-1}) vibrations are also detected on this sample. The Co_1Ni_1 IR spectra are similar to

those of Co_4Ni_1 due to co-deposition of nitrite and nitrate species. However, some subtle differences are observed. The separation between symmetrical and asymmetrical bands in the 1320–1420 cm^{-1} range becomes smaller over Co_1Ni_1 likely due to altered nitrate to nitrite ratios. Also, the water band at 1630 cm^{-1} and the chelating nitro band at 1190 cm^{-1} are weakened on Co_1Ni_1 as compared to those on Co_4Ni_1. Moreover, the shoulder band at 1286 on Co_1Ni_1 is attributed to monodentate nitrate [42] and another band at 1566 cm^{-1} is assigned to bidentate nitrate, respectively [43]. Overall, the IR bands observed on Co_1Ni_1 are in line with XPS analysis (Fig. 8c), which shows that nitrates are more dominant on Co_1Ni_1 than on Co_4Ni_1 and Co-pure. IR spectra for Co_1Ni_4 present a prominent band at 1384 cm^{-1} and a weak shoulder at 1286 cm^{-1}, corresponding to ionic nitrate and monodentate nitrate, respectively [44]. The bands on Ni-pure at 1525, 1286 and 971 cm^{-1} are attributed to monodentate nitrate [39]. Finally, we note that in the
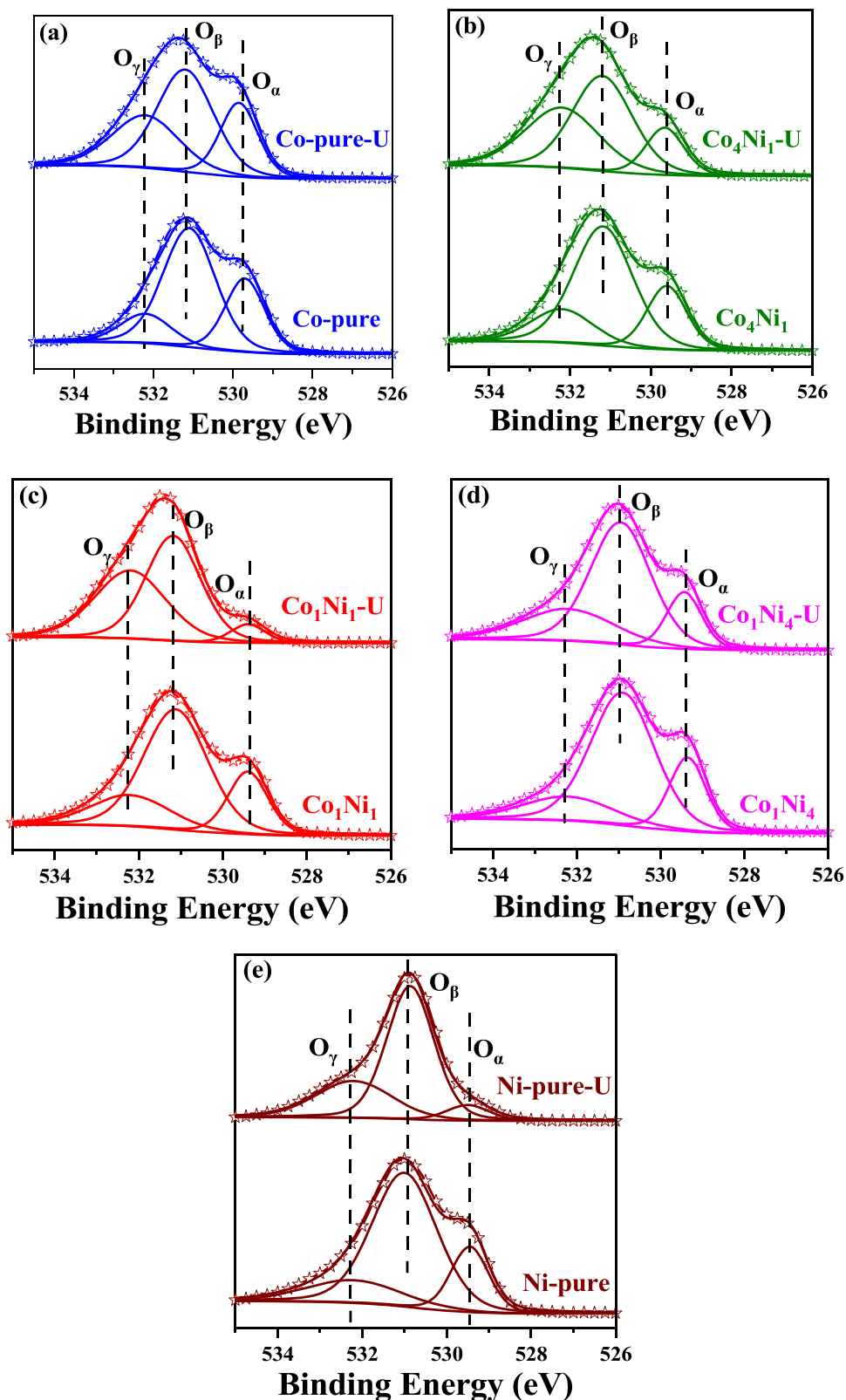
Fig. 9. Deconvoluted O 1 s XPS (a-e) spectra for fresh and used $Co_xNi_yO_z \cdot nH_2O$ materials.

1950–2100 cm^{-1} range, broad bands develop on Co-pure (2060 cm^{-1}), Co_4Ni_1 (2060 cm^{-1}) and Co_1Ni_1 (1955 cm^{-1}), but not on Co_1Ni_4 and Ni-pure. The nature of these bands is not entirely clear but could be attributed to vibrations of NO and NO_2 species held in the micropores of these materials [45,46]. To directly compare the 5 samples, Fig. 10f summarize the IR spectra acquired at 30 min of NO/O_2 exposure. Based on the relative peak intensities, the order of NO storage capacity follows $Co_1Ni_1 \approx Co_4Ni_1 >$ Co-pure $>$ Ni-pure $\approx Co_1Ni_4$. Such a trend is in reasonable consistency with their NO elimination performance measured under flow conditions (Fig. 1).

Table 3

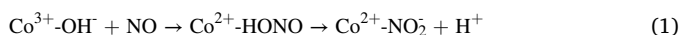Quantification of different oxygen species in fresh and used $Co_xNi_yO_z \cdot nH_2O$ materials.

Materials	O_α (%)	ΔO_α (%)	O_β (%)	ΔO_β (%)	O_γ (%)	ΔO_γ (%)
Co-pure	26.8	-3.77	60.7	-12.9	12.5	16.6
Co-pure-U	23.1		47.8		29.1	
Co_4Ni_1	21.8	-6.7	60.3	-12.6	17.9	19.3
Co_4Ni_1-U	15.1		47.7		37.2	
Co_1Ni_1	19.6	-13.9	62.5	-11.1	17.9	25.0
Co_1Ni_1-U	5.7		51.4		42.9	
Co_1Ni_4	20.2	-4.0	63.4	-3.5	16.4	7.5
Co_1Ni_4-U	16.2		59.9		23.9	
Ni-pure	18.5	-11.7	65.2	-0.5	16.3	12.2
Ni-pure-U	6.8		64.7		28.5	

Following the 30-min storage, the samples were subjected to TPD measurements to probe the nature of desorbed species. As shown in Fig. 11, Co-pure, Co_4Ni_1 and Co_1Ni_1 present weak desorption peaks at 105, 110 and 96 °C, respectively, which can be attributed to the release of NO or NO_2 trapped in micropores of these materials, i.e., species which are associated with the 1950–2100 cm^{-1} bands shown in Fig. 10. NO and NO_2 released at higher temperatures are due to nitrite/nitrate decomposition, and the desorption yields are consistent with the corresponding IR signal intensities shown in Fig. 10f. The NO desorption peaks are centered at 224, 220 and 235 °C for Co-pure, Co_4Ni_1 and Co_1Ni_1, respectively. These are assigned to the decomposition of nitrite species, i.e., the nitro compounds assigned in Fig. 10. The order of NO desorption quantity is as follows: Co-pure > Co_4Ni_1 > Co_1Ni_1. The NO_2 desorption peak at 270 °C and the NO desorption peak at 324 °C for Co-pure are jointly attributed to the decomposition of ionic nitrates. Similarly, the decompositions of ionic nitrates for Co_4Ni_1 and Co_1Ni_1 also lead to two desorption peaks: NO_2 desorption peak at lower temperature and NO desorption peak at higher temperature. For Co-pure, surprisingly, a pronounced NO desorption peak is observed at 481 °C. This is indexed to relatively stable ionic nitrate, which might be formed by the oxidation of nitro compounds during temperature ramping. Additionally, the weak NO desorption peak at 520 °C for Co_1Ni_4 belongs to the decomposition of relatively stable ionic nitrate. The NO and NO_2 desorption peaks for Ni-pure at around 377 °C are attributed to the decomposition of monodentate nitrate.

The combined XPS, DRIFTS and TPD analyses lead to a few important points worth discussing: (1) Based on comparisons between Co-pure and Ni-pure, it is clear that nitrite formation is associated with Co, and nitrate formation is associated with Ni. Upon nitrite/nitrate formation, there is clear decrease in the oxidation state of Co and Ni as evidenced from XPS, due to O_α and O_β consumption (Fig. 8). Such oxygen species are not readily replenished by gas phase O_2. (2) For Co_4Ni_1 and Co_1Ni_1, the situation becomes less clear: nitrates form on both materials but no Ni binding energy shift is found in either case. This leads to a postulation that the Ni component in these bimetallic hydrous oxides are highly efficient in activating O_2 so that the lattice oxygen consumed in NO oxidation is rapidly replenished by gas phase O_2, causing no measurable changes in Ni oxidation states. (3) There is a clear positive correlation between nitrite and water formation during NO storage. For Co-pure and Co_4Ni_1, large quantities of nitrite form accompanied by strongest 1630 cm^{-1} H_2O bending band (Fig. 10). For the other samples with less or no nitrite deposition, the 1630 cm^{-1} band becomes weak to even undetectable. Next, possible reaction mechanisms are proposed.
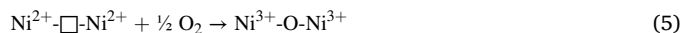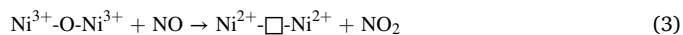
On Co-pure, based on the facts that O_β consumption overwhelms O_α and nitrite/H_2O formation overwhelms other deposits, likely reaction pathways are listed as follows:

$$Co^{3+}\text{-}OH^- + NO \rightarrow Co^{2+}\text{-}HONO \rightarrow Co^{2+}\text{-}NO_2^- + H^+ \quad (1)$$

$$Co^{3+}\text{-}OH^- + H^+ \rightarrow Co^{3+} + H_2O \quad (2)$$

In this case, continuous surface hydroxyls consumption and nitrite

deposition eventually lead to NO trapping efficiency decrease until saturation.

On Ni-pure, O_α consumption overwhelms O_β, nitrates rather than nitrites form, and NO_2 appears to be an intermediate for nitrate formation. This latter point follows since as the storage capacity decreases, NO_2 formation appears (Fig. 1). Considering these, the following reaction pathways are proposed ("$\square$" represents a lattice oxygen vacancy):

$$Ni^{3+}\text{-}O\text{-}Ni^{3+} + NO \rightarrow Ni^{2+}\text{-}\square\text{-}Ni^{2+} + NO_2 \quad (3)$$

$$Ni^{3+}\text{-}OH^- + NO_2 \rightarrow Ni^{2+}\text{-}HNO_3 \quad (4)$$

$$Ni^{2+}\text{-}\square\text{-}Ni^{2+} + \tfrac{1}{2} O_2 \rightarrow Ni^{3+}\text{-}O\text{-}Ni^{3+} \quad (5)$$

On this material, a quasi-steady-state NO_2 formation is reached by reactions (3) + (5), however, nitrate formation is governed by consumption of surface hydroxyls which are much less active than hydroxyls on Co-pure. Therefore, this material is much inferior to Co-pure in NO trapping.

Over Co_4Ni_1 and Co_1Ni_1, the co-deposition of nitrite and nitrate lead to a hypothesis that nitrites formed on Co are later oxidized by lattice oxygen on Ni:

$$Co^{2+}\text{-}NO_2^- + Ni^{3+}\text{-}O\text{-}Ni^{3+} \rightarrow Co^{2+}\text{-}NO_3^- + Ni^{2+}\text{-}\square\text{-}Ni^{2+} \quad (6)$$
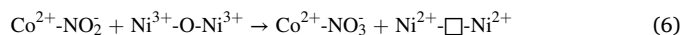
We note that reaction (6) is only a prototypical pathway describing synergy between Co and Ni in the bimetallic hydrous oxides. For example, whether Co and Ni mix at an atomic level (i.e., with the formation of Co-O-Ni linkages) is not known. If such moieties exist, then lattice oxygen within such species may also contribute NO storage. Also the effects of material morphology upon Ni introduction to Co, i.e., from spherical grains to sheet-like structures, are not known. Finally, the nitrate species formed during NO storage do not have to be bound to the metal cations. Fig. 10 clearly displays the presence of free nitrate species.

3.4. Regeneration of the materials

Upon NO_x storage, the materials described in the present study must be regenerated for repeated use. As shown in Fig. 11, the Co_xNi_y will need to be heated to ~400 °C to release all the trapped nitrite/nitrate. However, our previous study demonstrates that such poorly crystalline hydrated materials are unstable at such high temperatures, and will convert to their corresponding oxides and lose NO_x storage capacity [21]. We have demonstrated previously that CoOOH can be successfully regenerated by washing in $Na_2S_2O_8$ aqueous solution. This washing serves two purposes: first, the stored nitrite/nitrate will dissolve in water, and second, the reduced metal cations will be reoxidized (i.e., Co^{2+} oxidation back to Co^{3+}). Since Co_1Ni_1 material exhibits the most outstanding low-concentration NO removal performance, it was chosen here to demonstrate the effectiveness of this regeneration method. As shown in Fig. 12, NO removal performance of the regenerated Co_1Ni_1 (denoted Co_1Ni_1-R) remains essentially the same as its fresh counterpart. The IR spectra for fresh, used and regenerated Co_1Ni_1 exposed to NO/O_2 for 30 min were acquired, and the results are shown in Fig. S5. This demonstrates clearly that the NO adsorption capacity for used Co_1Ni_1 can be readily regenerated. To further reveal reusability, the Co_1Ni_1 catalyst regeneration was repeated four times, and the corresponding NO storage testing results are shown in Fig. S6. It is found that the catalyst remains essentially unchanged 100 % NO elimination durations with these regeneration cycles. However, the durations of NO removal efficiency drop from 100 % to 50 % become shortened with regeneration progression, indicating minor decay of the catalyst in each regeneration event.

Finally, we would like to point out that in practical applications, the Co-Ni hydrous oxide catalysts will likely be washcoated as monolithic catalysts. In addition to potential agglomeration or disintegration of the catalytically active phases, regeneration with $Na_2S_2O_8$ solution also

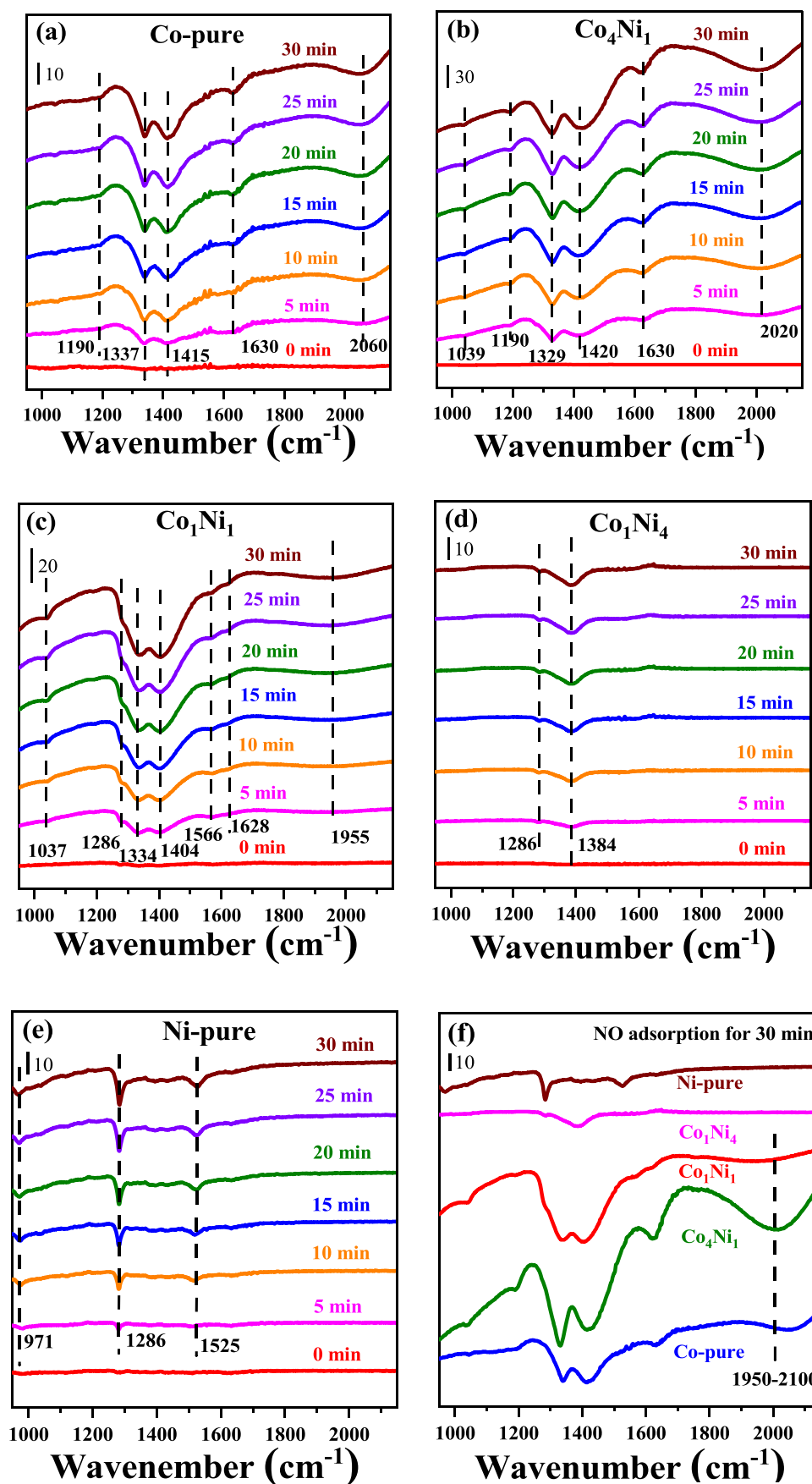**Fig. 10.** In situ DRIFT spectra of NO/O_2 adsorption on Co-pure (a), Co_4Ni_1 (b), Co_1Ni_1 (c), Co_1Ni_4 (d) and Ni-pure (e); IR spectra at 30 min of NO/O_2 exposure on $Co_xNi_yO_z \cdot nH_2O$ materials (f).
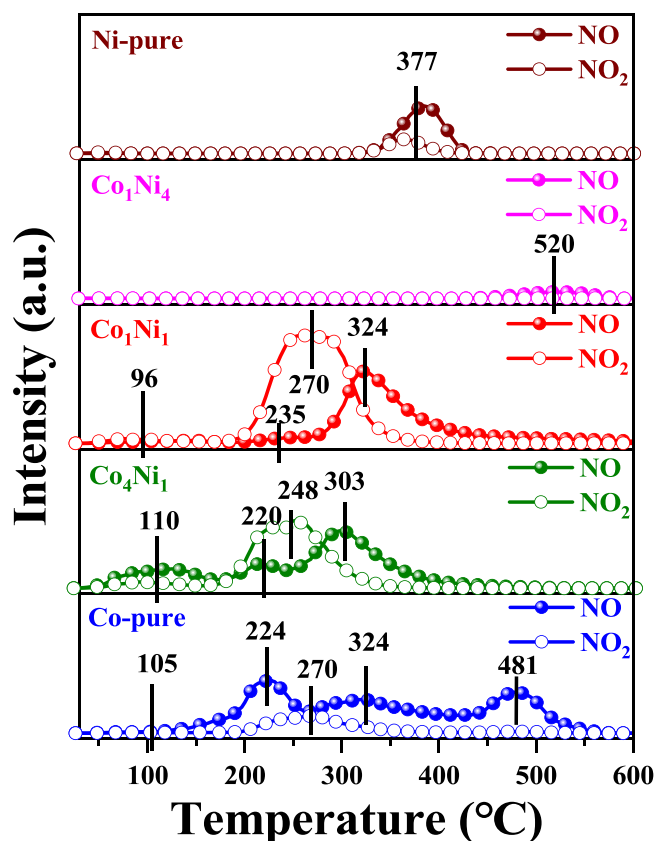
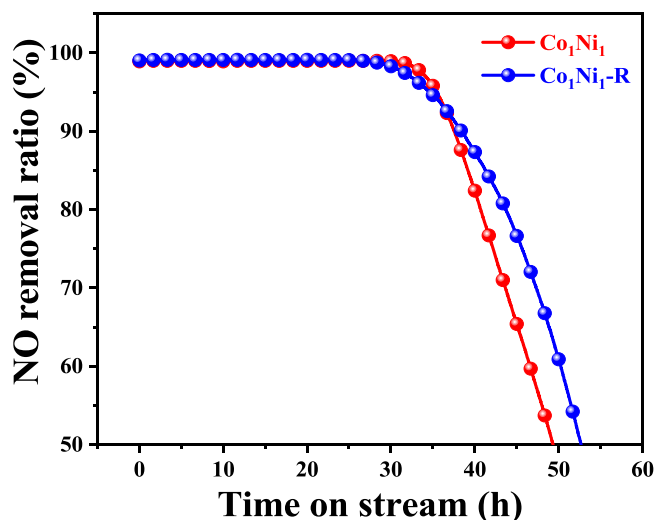**Fig. 11.** NO+O$_2$-TPD profiles on Co$_x$Ni$_y$O$_z$·nH$_2$O materials.

Fig. 12. Comparison of low-concentration NO removal performance at ambient temperature on fresh and regenerated Co$_1$Ni$_1$ materials. (c$_{NO}$ = 10 ppm, c$_{O2}$ = 21 vol%, WHSV = 120,000 mL·g^{-1}·h^{-1}, T = 25 ℃).

becomes more challenging. One possible way is to use a low Na$_2$S$_2$O$_8$ solution flow to rinse the monolithic catalyst. In this case, it is important to use a good binder to avoid the active phases to be washed away. Based on the current study, Na$_2$S$_2$O$_8$ solution washing leads to wastewater containing sulfate and nitrate species. It is also possible that with repeated uses, some Co and Ni can also leach into the wastewater. Potential environmental impacts from wastewater should be considered for practical applications.

4. Conclusion

Co-Ni bimetallic hydrous oxides (Co$_x$Ni$_y$O$_z$·nH$_2$O) are synthesized as trapping materials/catalysts for the elimination of low concentration NO in air. In these materials, the two metals stay primarily as intimately mixed CoOOH and NiOOH moieties. The balance between near-spherical and sheet-like grains, strongly influenced by Co/Ni atomic ratio, is key for high surface area and low crystallinity of these materials. Although small quantities of NO and NO$_2$ can be trapped in pores of these materials, NO$_x$ storage is primarily via nitrite and nitrate formation. Based on in situ DRIFTS, XPS and temperature-programmed desorption studies, nitrite formation is found to be associated with Co, and nitrate formation is found to be associated with Ni. A synergy is also identified where nitrite formed on Co is further oxidized to nitrate by lattice oxygen on Ni. Based on these findings, possible nitrite and nitrate formation chemistries are proposed. Some of the bimetallic hydrous oxides studied here, e.g., Co$_1$Ni$_1$, display remarkable NO trapping efficiency at ambient temperature, and thus, hold great application potentials. Finally, even though thermal regeneration cannot be applied to these poorly crystalline materials, washing with Na$_2$S$_2$O$_8$ aqueous solution readily restores their trapping capacity.

CRediT authorship contribution statement

Bo Lin: Conceptualization, Methodology, Investigation, Writing - original draft. **Ziwei Bao**: Investigation. **Aiyong Wang:** Visualization, Writing - original draft. **Yuanqing Ding:** Validation. **Wangcheng Zhan:** Formal analysis. **Li Wang:** Conceptualization, Writing - review & editing. **Yun Guo:** Resources, Funding acquisition. **Qiguang Dai:** Methodology. **Yanglong Guo:** Supervision, Writing - review & editing. **Feng Gao:** Conceptualization, Writing - review & editing.

Declaration of Competing Interest

The authors declare that they have no known competing financial interests or personal relationships that could have appeared to influence the work reported in this paper.

Data availability

Data will be made available on request.

Acknowledgments

Appendix A. Supporting information

Supplementary data associated with this article can be found in the online version at doi:10.1016/j.apcatb.2023.122984.

References

[1] E. Bello, V.J. Margarit, E.M. Gallego, F. Schuetze, C. Hengst, A. Corma, M. Moliner, Deactivation and regeneration studies on Pd-containing medium pore zeolites as passive NO$_x$ adsorbers (PNAs) in cold-start applications, Micropor. Mesopor, Microporous Mesoporous Mater. 302 (2020), 110222.

[2] J.R. Theis, C.K. Lambert, An assessment of low temperature NO adsorbers for cold-start NO control on diesel engines, Catal. Today 258 (2015) 367–377.

[3] M. Weilenmann, J.Y. Favez, R. Alvarez, Cold-start emissions of modern passenger cars at different low ambient temperatures and their evolution over vehicle legislation categories, Atmos. Environ. 43 (2009) 2419–2429.

[4] J. Zhu, Y. Wei, W. Chen, Z. Zhao, A. Thomas, Graphitic carbon nitride as a metal-free catalyst for NO decomposition, Chem. Commun. 46 (2010) 6965–6967.

[5] F. Gao, E.D. Walter, E.M. Karp, J. Luo, R.G. Tonkyn, J.H. Kwak, J. Szanyi, C.H. F. Peden, Structure–activity relationships in NH$_3$-SCR over Cu-SSZ-13 as probed by reaction kinetics and EPR studies, J. Catal. 300 (2013) 20–29.

[6] X. Li, X. Li, T. Zhu, Y. Peng, J. Li, J. Hao, Extraordinary deactivation offset effect of arsenic and calcium on CeO$_2$-WO$_3$ SCR catalysts, Environ. Sci. Technol. 52 (2018) 8578–8587.

[7] B. Meng, Z. Zhao, X. Wang, J. Liang, J. Qiu, Selective catalytic reduction of nitrogen oxides by ammonia over Co$_3$O$_4$ nanocrystals with different shapes, Appl. Catal. B 129 (2013) 491–500.

[8] Y.J. Kim, H.J. Kwon, I. Heo, I.-S. Nam, B.K. Cho, J.W. Choung, M.-S. Cha, G.K. Yeo, Mn–Fe/ZSM5 as a low-temperature SCR catalyst to remove NO$_x$ from diesel engine exhaust, Appl. Catal. B 126 (2012) 9–21.

[9] H. Yuan, J. Chen, Y. Guo, H. Wang, P. Hu, Insight into the superior catalytic activity of MnO$_2$ for low-content NO oxidation at room temperature, J. Phys. Chem. C 122 (2018) 25365–25373.

[10] J.P.S. Sousa, M.F.R. Pereira, J.L. Figueiredo, NO oxidation over nitrogen doped carbon xerogels, Appl. Catal. B 125 (2012) 398–408.

[11] I. Mochida, N. Shirahama, S. Kawano, Y. Korai, A. Yasutake, M. Tanoura, S. Fujii, M. Yoshikawa, NO oxidation over activated carbon fiber (ACF). Part 1. Extended kinetics over a pitch based ACF of very large surface area, Fuel 79 (2000) 1713–1723.

[12] S. Andonova, V. Marchionni, L. Lietti, L. Olsson, Micro-calorimetric studies of NO$_2$ adsorption on Pt/BaO-supported on γ-Al$_2$O$_3$ NO$_x$ storage and reduction (NSR) catalysts - impact of CO$_2$, Mol. Catal. 436 (2017) 43–52.

[13] T. Selleri, F. Gramigni, I. Nova, E. Tronconi, NO oxidation on Fe- and Cu-zeolites mixed with BaO/Al$_2$O$_3$: free oxidation regime and relevance for the NH$_3$-SCR chemistry at low temperature, Appl. Catal. B 225 (2018) 324–331.

[14] Z. Shu, Y. Chen, W. Huang, X. Cui, L. Zhang, H. Chen, G. Zhang, X. Fan, Y. Wang, G. Tao, D. He, J. Shi, Room-temperature catalytic removal of low-concentration NO over mesoporous Fe-Mn binary oxide synthesized using a template-free approach, Appl. Catal. B 140-141 (2013) 42–50.

[15] Z. Shu, W. Huang, Z. Hua, L. Zhang, X. Cui, Y. Chen, H. Chen, C. Wei, Y. Wang, X. Fan, H. Yao, D. He, J. Shi, Template-free synthesis of mesoporous X-Mn (X = Co, Ni, Zn) bimetal oxides and catalytic application in the room temperature removal of low-concentration NO, J. Mater. Chem. A 1 (2013) 10218.

[16] J. Wang, J. Zhu, X. Zhou, Y. Du, W. Huang, J. Liu, W. Zhang, J. Shi, H. Chen, Nanoflower-like weak crystallization manganese oxide for efficient removal of low-concentration NO at room temperature, J. Mater. Chem. A 3 (2015) 7631–7638.

[17] Y. Du, W. Huang, Z. Hua, Y. Wang, X. Cui, M. Wu, Z. Shu, L. Zhang, J. Wang, H. Chen, J. Shi, A facile ultrasonic process for the preparation of Co$_3$O$_4$ nanoflowers for room-temperature removal of low-concentration NO$_x$, Catal. Commun. 57 (2014) 73–77.

[18] S. Liu, M. Zhang, Y. Huang, K. Zhao, Z. Gao, M. Wu, Y. Dong, T. Wang, J. Shi, D. He, A novel chromic oxide catalyst for NO oxidation at ambient temperature, RSC Adv. 4 (2014), 29180.

[19] A. Wang, B. Lin, H. Zhang, M.H. Engelhard, Y. Guo, G. Lu, C.H.F. Peden, F. Gao, Ambient temperature NO oxidation over Cr-based amorphous mixed oxide catalysts: effects from the second oxide components, Catal. Sci. Technol. 7 (2017) 2362–2370.

[20] A. Wang, Y. Guo, F. Gao, C.H.F. Peden, Ambient-temperature NO oxidation over amorphous CrO$_x$-ZrO$_2$ mixed oxide catalysts: significant promoting effect of ZrO$_2$, Appl. Catal. B 202 (2017) 706–714.

[21] B. Lin, A. Wang, Y. Guo, Y. Ding, W. Zhan, L. Wang, Y. Guo, F. Gao, Elimination of NO pollutant in semi-enclosed spaces over sodium-promoted cobalt oxyhydroxide (CoOOH) by oxidation and adsorption mechanism, Appl. Catal. B 279 (2020), 119404.

[22] B. Lin, A. Wang, Y. Guo, Y. Ding, Y. Guo, L. Wang, W. Zhan, F. Gao, Ambient temperature NO adsorber derived from pyrolysis of Co-MOF (ZIF-67), ACS Omega 4 (2019) 9542–9551.

[23] T. Pauporté, L. Mendoza, M. Cassir, M.C. Bernard, J. Chivot, Direct low-temperature deposition of crystallized CoOOH films by potentiostatic electrolysis, J. Electrochem. Soc. 152 (2005) C49–C53.

[24] Y. Jin, S. Huang, X. Yue, H. Du, P.K. Shen, Mo- and Fe-modified Ni(OH)$_2$/NiOOH nanosheets as highly active and stable electrocatalysts for oxygen evolution reaction, ACS Catal. 8 (2018) 2359–2363.

[25] Y. Jin, S. Huang, X. Yue, C. Shu, P.K. Shen, Highly stable and efficient non-precious metal electrocatalysts of Mo-doped NiOOH nanosheets for oxygen evolution reaction, Int. J. Hydrog. Energy 43 (2018) 12140–12145.

[26] S. Song, H. Bao, X. Lin, X.L. Du, J. Zhou, L. Zhang, N. Chen, J. Hu, J.Q. Wang, Molten salt-assisted synthesis of bulk CoOOH as a water oxidation catalyst, J. Energy Chem. 42 (2020) 5–10.

[27] L. Yan, B. Zhang, Z. Liu, J. Zhu, Synergy of copper doping and oxygen vacancies in porous CoOOH nanoplates for efficient water oxidation, Chem. Eng. J. 405 (2021), 126198.

[28] J. Lin, H. Wang, Y. Yan, X. Zheng, H. Jia, J. Qi, J. Cao, J. Tu, W. Fei, J. Feng, Core-branched CoSe$_2$/Ni$_{0.85}$Se nanotube arrays on Ni foam with remarkable electrochemical performance for hybrid supercapacitors, J. Mater. Chem. A 6 (2018) 19151–19158.

[29] M.C. Biesinger, B.P. Payne, A.P. Grosvenor, L.W.M. Lau, A.R. Gerson, R.S.C. Smart, Resolving surface chemical states in XPS analysis of first row transition metals, oxides and hydroxides: Cr, Mn, Fe, Co and Ni, Appl. Surf. Sci. 257 (2011) 2717–2730.

[30] S. Klemenz, J. Schuch, S. Hawel, A.M. Zieschang, B. Kaiser, W. Jaegermann, B. Albert, Synthesis of a highly efficient oxygen-evolution electrocatalyst by incorporation of iron into nanoscale cobalt borides, ChemSusChem 11 (2018) 3150–3156.

[31] Q. Zhang, D. He, X. Li, W. Feng, C. Lyu, Y. Zhang, Mechanism and performance of singlet oxygen dominated peroxymonosulfate activation on CoOOH nanoparticles for 2,4-dichlorophenol degradation in water, J. Hazard. Mater. 384 (2020), 121350.

[32] A. Yoshida, W. Shen, T. Eda, R. Watanabe, T. Ito, S. Naito, NO$_x$ storage/reduction over alkali-metal-nitrate impregnated titanate nanobelt catalysts and investigation of alkali metal cation migration using XPS, Catal. Today 184 (2012) 78–82.

[33] Y.P. Zhu, T.Y. Ma, M. Jaroniec, S.Z. Qiao, Self-templating synthesis of hollow Co$_3$O$_4$ microtube arrays for highly efficient water electrolysis, Angew. Chem. Int. Ed. 56 (2017) 1324–1328.

[34] P. Tan, B. Chen, H. Xu, W. Cai, W. He, M. Ni, In-situ growth of Co$_3$O$_4$ nanowire-assembled clusters on nickel foam for aqueous rechargeable Zn-Co$_3$O$_4$ and Zn-air batteries, Appl. Catal. B 241 (2019) 104–112.

[35] L.T. Gonzalez, F.E. Longoria-Rodriguez, M. Sanchez-Dominguez, C. Leyva-Porras, K. Acuna-Askar, B.I. Kharissov, A. Arizpe-Zapata, J.M. Alfaro-Barbosa, Seasonal variation and chemical composition of particulate matter: A study by XPS, ICP-AES and sequential microanalysis using Raman with SEM/EDS, J. Environ. Sci. 74 (2018) 32–49.

[36] T. Herranz, X. Deng, A. Cabot, Z. Liu, M. Salmeron, In situ XPS study of the adsorption and reactions of NO and O$_2$ on gold nanoparticles deposited on TiO$_2$ and SiO$_2$, J. Catal. 283 (2011) 119–123.

[37] K. Nakamoto, J. Fujita, H. Murata, The infrared spectra of nitro and nitrito complexes, J. Am. Chem. Soc. 80 (1958) 4817–4823.

[38] Y. Liu, Y. Ma, D. Weng, X. Wu, Z. Si, Pt@g-C$_3$N$_4$/CeO$_2$ photocatalyst for the remediation of low concentration NO at room temperature, Prog. Nat. Sci.: Mater. Int. 30 (2020) 308–311.

[39] K.I. Hadjiivanov, Identification of neutral and charged N$_x$O$_y$ surface species by IR spectroscopy, Catal. Rev. 42 (2000) 71–144.

[40] S. Ashihara, S. Fujioka, K. Shibuya, Temperature dependence of vibrational relaxation of the OH bending excitation in liquid H$_2$O, Chem. Phys. Lett. 502 (2011) 57–62.

[41] I. Nova, L. Castoldi, F. Prinetto, V. DalSanto, L. Lietti, E. Tronconi, P. Forzatti, G. Ghiotti, R. Psaro, S. Recchia, NO$_x$ adsorption study over Pt-Ba/alumina catalysts: FT-IR and reactivity study, Top. Catal. 30-31 (2004) 1–4.

[42] M. Qiu, S. Zhan, H. Yu, D. Zhu, S. Wang, Facile preparation of ordered mesoporous MnCo$_2$O$_4$ for low-temperature selective catalytic reduction of NO with NH$_3$, Nanoscale 7 (2015) 2568–2577.

[43] Y. Chi, S.S.C. Chuang, Infrared and TPD studies of nitrates adsorbed on Tb$_4$O$_7$, La$_2$O$_3$, BaO, and MgO/γ-Al$_2$O$_3$, J. Phys. Chem. B 104 (2000) 4673–4683.

[44] J. Ding, C. Yu, J. Lu, X. Wei, W. Wang, G. Pan, Enhanced CO$_2$ adsorption of MgO with alkali metal nitrates and carbonates, Appl. Energy 263 (2020), 114681.

[45] C.P. Theologides, G.G. Olympiou, P.G. Savva, K. Kapnisis, A. Anayiotos, C.N. Costa, Mechanistic aspects (SSITKA-DRIFTS) of the catalytic denitrification of water with hydrogen on Pd-Cu supported catalysts, Appl. Catal. B 205 (2017) 443–454.

[46] A. Łamacz, A. Krztoń, G. Djéga-Mariadassou, Study on the selective catalytic reduction of NO with toluene over CuO/CeZrO$_2$. A confirmation for the three-function model of HC-SCR using the temperature programmed methods and in situ DRIFTS, Appl. Catal. B 142-143 (2013) 268–277.